中国激光

基于腔内球差选模的超高阶拉盖尔-高斯涡旋激光

王爱华[1,2]，李锦辉[3]，盛泉[1,2*]，耿婧旎[1,2]，付士杰[1,2]，史伟[1,2**]，姚建铨[1,2]

[1]天津大学精密仪器与光电子工程学院，天津 300072；

[2]天津大学光电信息技术教育部重点实验室，天津 300072；

[3]东南大学成贤学院，江苏 南京 210088

摘要 利用不同阶拉盖尔-高斯(LG)模式激光具有不同光束尺寸的特性，在激光谐振腔内使用短焦距透镜引入球差，使各阶LG模式激光的空间光路发生分离，从而实现对高阶横模的选择并产生高阶LG模式涡旋激光输出。通过对高阶LG模式激光的聚焦特性和透镜球差进行分析计算，给出了高阶$LG_{0,\pm m}$模式涡旋激光的角向指数(m)随谐振腔参数变化的理论模型。搭建端面泵浦的1064 nm Nd∶YVO_4激光器开展了实验研究，在2.06 W泵浦功率下获得了角向指数可便捷调控且m最高可达到280的超高阶$LG_{0,\pm m}$涡旋激光输出。实验产生的超高阶涡旋激光具有良好的功率和模式稳定性，模式变化规律与理论计算结果相符。通过增加泵浦功率或优化泵浦交叠以提高激光增益，理论上可以产生任意高阶的涡旋激光输出。研究结果为超高阶LG模式涡旋激光的产生提供了参考。

关键词 激光光学；拉盖尔-高斯模式；涡旋激光；模式选择；高阶横模；球差

中图分类号 TN248.1 **文献标志码** A **DOI**：10.3788/CJL230543

1 引 言

拉盖尔-高斯(LG)模式的涡旋激光在光通信、量子信息、粒子操控、激光加工等领域中有广泛的应用[1-4]。LG模式的角向指数(m)决定了光子的轨道角动量，可调谐的大轨道角动量有助于提升光通信应用中的信道容量和信息编码量[5-6]，在量子纠缠和高精度空间测量方面也有广阔的应用前景[7-8]。因此，可控的高阶LG模式涡旋光产生方法成为激光物理领域的研究热点。产生LG模式激光的方法主要分为腔外转换和腔内直接激发两类。腔外转换是在激光谐振腔外利用相位板或柱透镜等器件对高斯或厄米-高斯激光进行变换，得到LG涡旋光束[9-11]；腔内直接激发则是控制激光谐振腔内特定模式的增益或损耗，使高阶LG模式振荡输出[12]。与腔外转换的方法相比，腔内直接激发系统简洁紧凑、涡旋光束质量更好[13]。腔内直接激发产生高阶LG的方法一般有环形泵浦光[14-15]、腔内相位模板调制[16]以及使用带有缺陷点的腔镜[17-18]等。各类激发方法有不同的优缺点，相应的应用方式和场景也不同。然而，腔内直接激发方法很少能够获得超高阶的LG模式激光输出。2018年，Qiao等[19]基于缺陷点反射镜获得了最高角向指数m达到288的实验结果。除此之外，其他相关报道的最高阶输出多在50阶以下。

不同阶LG模式具有不同的光斑尺寸，如果在谐振腔内引入较大的球差，各阶LG模式的光路在空间上就会发生分离，使得选择高阶模式、实现涡旋激光输出成为可能。2010，Thirugnanasambandam等[20]通过在激光谐振腔内插入短焦距透镜引入了球差，实现了LG模式的振荡输出，通过将激光谐振腔拉长至1 m左右，加强球差对模式的区分度，获得了径向指数(p)最高为12、角向指数m最大为28的$LG_{p,\pm m}$模式输出。近期，我们通过压窄谐振腔稳区来加强球差对模式的区分能力，基于更为紧凑的腔结构实现了最高角向指数m为95的$LG_{0,\pm m}$输出以及径向指数$p\neq0$的输出[21-22]。基于腔内球差选模实现高阶LG模式输出无需相位板和调制器等额外器件，也避免了缺陷点反射镜制备和泵浦整形等操作，实现方法相对简单且阶数能够在较大范围内调控。本文通过对高阶LG模式聚焦特性的分析，得到了腔内透镜球差与激光模式之间关系的理论模型；通过优化实验参数，实现了m最高可达280的超高阶$LG_{0,\pm m}$涡旋光输出。

2 实验装置和理论分析

图1为实验光路示意图。所用泵浦源为波长为878.6 nm的光纤耦合输出半导体激光器，其纤芯直径为200 μm、数值孔径为0.14。泵浦光经过耦合器聚焦到激光晶体的前端面，泵浦光斑半径为～120 μm；所用

收稿日期：2023-02-17；**修回日期**：2023-03-26；**录用日期**：2023-04-11；**网络首发日期**：2023-04-21

基金项目：国家自然科学基金(61975146，62105240，62075159)

通信作者：*shengquan@tju.edu.cn；**shiwei@tju.edu.cn

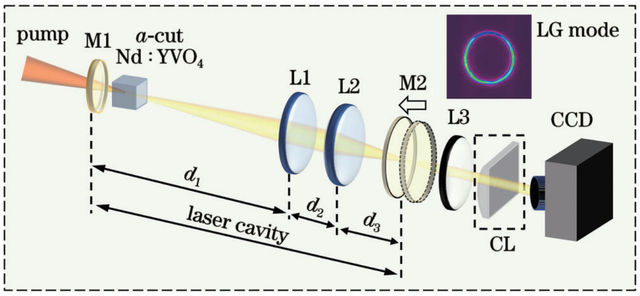

图1 超高阶LG模式激光器光路示意图

Fig. 1 Optical path diagram of ultra-high-order LG mode laser

激光晶体为尺寸为3 mm×3 mm×5 mm、Nd原子数分数为0.5%的a切割Nd:YVO_4晶体。谐振腔由凹面曲率半径为50 mm的平凹全反镜M1和平面输出镜M2组成，其中M1的镀膜对878.6 nm泵浦光高透、对1064 nm激光高反，1064 nm激光在M2镀膜上的透过率为T=10%，激光晶体靠近M1放置。腔内插入一片焦距为150 mm的平凸透镜L1和一片焦距为51.8 mm的双凸透镜L2。L1与激光晶体的距离为d_1=155 mm，束腰位于激光晶体附近的振荡光束经过L1准直后近似平行光并入射L2，L1和L2的间距为d_2=20 mm。在透镜L2球差的作用下，光斑尺寸越大的模式受到的会聚作用越强，因此具有环状光强分布的不同尺寸的各阶$LG_{0,\pm m}$模式的空间光路发生分离，为模式选择提供了便利。输出镜M2被放置在螺旋测微器驱动的位移台上，与L2的间距(d_3)约等于L2的焦距，并可以通过螺旋测微器进行微调。在谐振腔外使用焦距为200 mm的透镜L3对输出的高阶LG模式激光进行聚焦，在聚焦后的光束束腰处用电荷耦合器件(CCD)相机记录其远场光斑，而在束腰瑞利距离之外(实验中在束腰前～50 mm处)记录的光斑即为近场光斑。由于在谐振腔中未引入对LG模式手性的选择，产生的高阶LG模式同时含有角向指数分别为$+m$和$-m$的成分，在透镜L3之后使用一片焦距为100 mm的柱透镜(CL)将LG模式变换为厄米-高斯(HG)模式以观察$+m$和$-m$成分的光强比例。激光功率使用激光功率计表头和探头进行记录。

在高阶LG模式激光传输和变换的过程中，其q参数与基模高斯光束的q参数一样符合ABCD矩阵规律[23]。光束经过焦距为f的透镜聚焦后，其束腰位置与透镜表面的距离(l')为

$$l'=f+\frac{f^2(l-f)}{(l-f)^2+\left(\frac{\pi W_{p,m}^2}{\lambda M^2}\right)^2}=f+\frac{f^2(l-f)}{(l-f)^2+\left(\frac{\pi w_0^2}{\lambda}\right)^2}, \tag{1}$$

式中：λ为LG激光波长；M为光束质量因子；l为光束未经透镜聚焦前的束腰与透镜表面的距离；$W_{p,m}$为由光强二阶矩定义的LG光束半径；w_0为相应的基模高斯光束半径。$W_{p,m}$和w_0的关系为$W_{p,m}=w_0M=w_0\sqrt{2p+|m|+1}$。在实验中，LG光束经过透镜L1后得到了良好的准直，在透镜L2处的波前曲率半径趋于无穷，则其q参数近似为

$$\frac{1}{q}=-\frac{\mathrm{i}\lambda M^2}{\pi W_{p,m}^2}。 \tag{2}$$

经过ABCD矩阵传输规律变换，近似得到l'与透镜L2焦距f的关系式为

$$l'==f-\frac{f}{1+\frac{\pi^2 w_0^4}{\lambda^2 f^2}}。 \tag{3}$$

考虑L2的球差，对于尺寸不同的各阶$LG_{0,\pm m}$入射光束来说，透镜的焦距f不再是一个常数，而是随入射光高(h)变化的有效焦距f_{2_eff}。用Zemax软件计算得到标称焦距为51.8 mm的双凸透镜L2的有效焦距f_{2_eff}随入射光高h的变化如图2所示，透镜对光束的会聚作用随入射光高的增大而变强，当h从0增大至12 mm时，实际焦距从51.8 mm缩短至～47.2 mm。用三次多项式拟合二者关系：

$$f_{2\_\mathrm{eff}}\approx 51.80887-0.01322h-0.0256h^2-0.000487504h^3。 \tag{4}$$

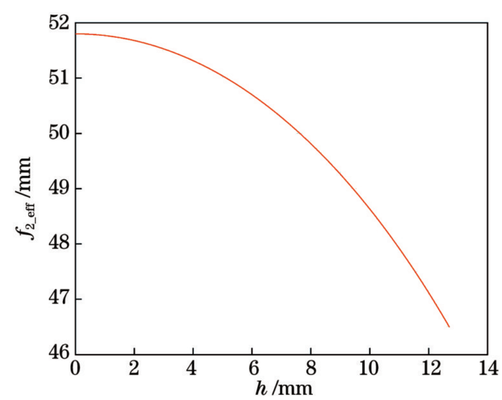

图2 f_{2_eff}随h的变化

Fig. 2 f_{2_eff} versus h

由此可知，具有环状光强分布的$LG_{0,\pm m}$光束经过L2聚焦后，其光束束腰的实际位置与f_{2_eff}有关，而f_{2_eff}又由$LG_{0,\pm m}$光束的光斑尺寸(模式阶数)决定。透镜L2和激光输出镜M2构成"猫眼"逆反射结构，由于M2镜为平面镜，只有束腰落在其反射面上的模式才能够得到良好的反馈，而离焦的模式则出现较大的损耗而不能起振[24-25]，因此，通过微调输出镜M2的位置，就能实现对$LG_{0,\pm m}$模式阶数的调控：缩短d_3，则光斑尺寸更大、f_{2_eff}更短的模式合焦，腔内振荡的激光变为更高阶的$LG_{0,\pm m}$模式，反之亦然。需要说明的是，此处决定f_{2_eff}的光斑尺寸并非上文中由光强二阶矩定义的LG光束半径$W_{p,m}=w_0(2p+m+1)^{1/2}$，而是其最大光强位置$W_{\max}$。$W_{\max}$更能反映LG模式光束经过透镜时实际

受到的会聚作用。在柱坐标系(r,θ,z)下，LG模式激光的电场分布描述[26]为

$$u_{p,m}(r,\theta,z)=\sqrt{\frac{2p!}{\pi(p+|m|)!}}\times\frac{1}{w(z)}\times\left[\frac{\sqrt{2}\,r}{w(z)}\right]^{|m|}\times L_p^{|m|}\left[\frac{2r^2}{w(z)^2}\right]\times\exp\left[-\frac{r^2}{w(z)^2}\right]\times$$
$$\exp(\mathrm{i}kz)\exp\left[\frac{\mathrm{i}kr^2z}{2(z^2+z_R^2)}\right]\exp\left[-\mathrm{i}(2p+|m|+1)\arctan\frac{z}{z_R}\right]\exp(\mathrm{i}m\theta),\tag{5}$$

式中：k为波数；$w(z)$为基模在z处的光束半径，$w(z)=w_0\sqrt{1+(z/z_R)^2}$；$z_R$为瑞利距离；$\exp(-\mathrm{i}m\theta)$为携带轨道角动量的螺旋相位项；$L_p^{|m|}[2r^2/w(z)^2]$为广义拉盖尔多项式。

根据式(5)计算得到的径向指数$p=0$时$LG_{0,\pm m}$模式的光斑尺寸$W_{p,m}$和其最大光强位置W_{max}随m的变化规律(对基模光斑半径作归一化处理)如图3所示，可见W_{max}明显小于$W_{p,m}$，在$m>10$时W_{max}只有$W_{0,m}$的～70%。根据w_0确定各阶W_{max}后，代入式(4)中的光高h，即得到各阶$LG_{0,\pm m}$模式实际的f_{2_eff}，再将其代入式(3)就可以计算各阶模式经过透镜L2聚焦后的束腰位置。也就是说，输出镜M2位于相应位置时能够产生该高阶$LG_{0,\pm m}$模式的激光输出。

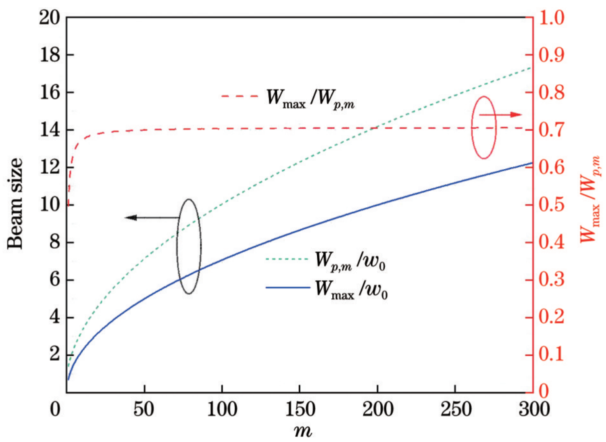

图3 $W_{p,m}/w_0$、W_{max}/w_0、$W_{max}/W_{p,m}$随m的变化

Fig. 3 $W_{p,m}/w_0$, W_{max}/w_0, and $W_{max}/W_{p,m}$ versus m

3 实验结果与讨论

实验中首先调节激光谐振腔使其输出为基模且功率最大，之后逐渐将M2向透镜L2方向移动，即缩短d_3，可以观察到激光输出由基模逐渐变为多模的平顶光再变为空心的多模光束(近远场分布不一致)，随后变为近远场分布一致的单一高阶$LG_{0,\pm m}$模式[27]；角向指数m随d_3的减小而逐渐增大。在2.06 W入射泵浦功率下，d_3为51.48 mm和48.91 mm时获得的$LG_{0,\pm 38}$和$LG_{0,\pm 280}$分别为最低阶和最高阶的单模输出，继续缩短d_3则激光器不能出光。图4给出了实验中记录的典型$LG_{0,\pm m}$模式激光经过腔外聚焦透镜聚焦后的近场、远场以及经过柱透镜变换的光斑图。其中光斑均为相机直接输出的光斑图像截图，未经任何处理，可见产生的$LG_{0,\pm m}$模式涡旋光具有很好的模式纯度。如前所述，由于谐振腔未引入对LG模式手性的选择，激光输出含有强度相近的角向指数分别为$+m$和$-m$的成

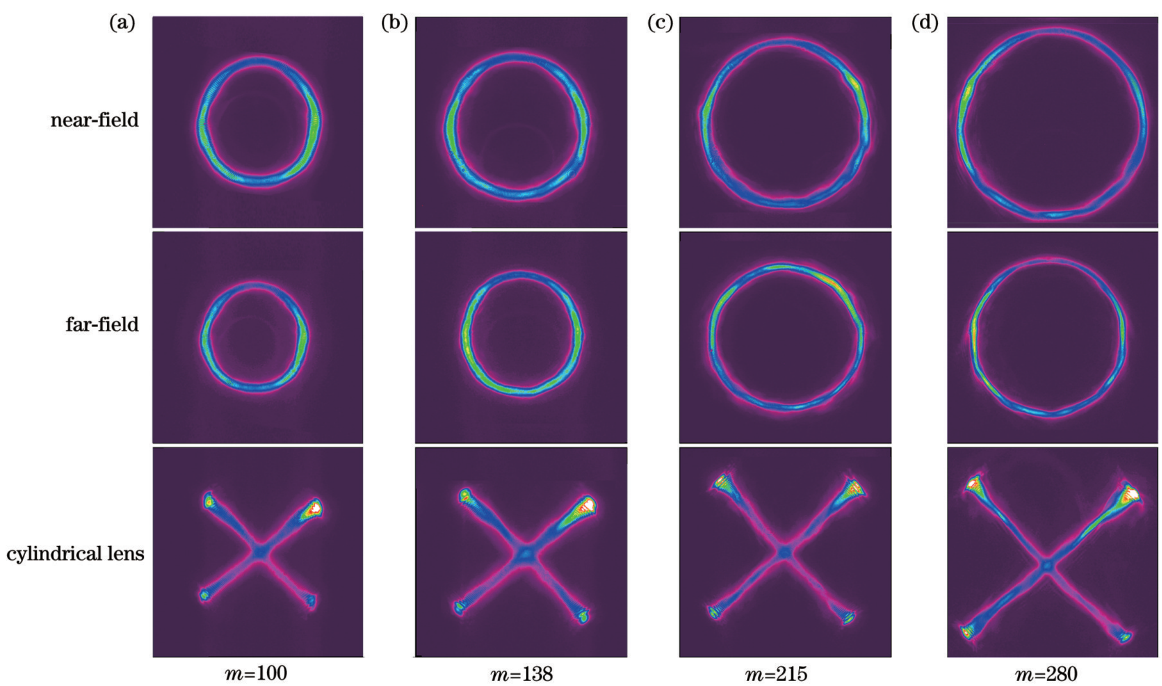

图4 在2.06 W泵浦功率下获得的典型高阶$LG_{0,\pm m}$模式激光的光斑图样

Fig. 4 Spot patterns of typical high-order $LG_{0,\pm m}$ mode laser obtained at pump power of 2.06 W

分，两者相干叠加形成花瓣状光斑，其角向的节线数即为角向指数 m。经柱透镜变换后得到的两个相互正交的强度相近的HG模式也验证了这一点。由ABCD矩阵计算得到的透镜L2处的基模光斑半径为~820 μm，根据式(3)~(5)计算各阶 $LG_{0,\pm m}$ 模式的 W_{max} 和对应的 f_{2_eff}，得到束腰的理论位置，如图5虚线所示，与圆圈所示的实验结果相吻合。

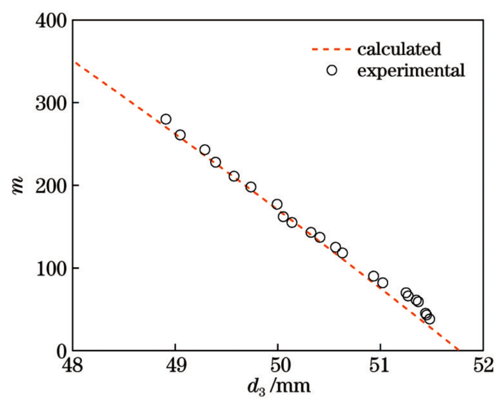

图5　m 随 d_3 的变化

Fig. 5　m versus d_3

图6给出了几个典型模式的输出功率曲线。在泵浦功率增加到3 W的过程中，激光模式保持不变，m 为85、106、138、146、230和280的 $LG_{0,\pm m}$ 模式的激光斜效率分别为24.6%、22.2%、20.6%、19.5%、14.4%和11.1%。高阶模式效率的下降一方面是由于振荡激光与泵浦光交叠的下降，另一方面光束尺寸和球差的增大使得合焦振荡的模式自身也引入了更高的损耗，这也是2.06 W泵浦功率下最高径向指数 m 被限制在280的原因。进一步增加泵浦功率以提高激光增益，理论上能够获得更高阶的 $LG_{0,\pm m}$ 模式激光输出。图7给出了 $LG_{0,\pm 138}$ 和 $LG_{0,\pm 230}$ 模式的输出功率在60 s内的波动情况，结果显示，激光器的功率稳定性较好，在此过程中也未观察到横模的跳变，其中RMS为均方根。

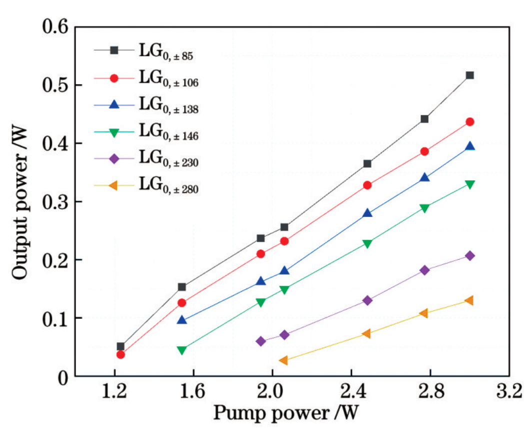

图6　不同 m 下 $LG_{0,\pm m}$ 模式激光的输出功率曲线

Fig. 6　Output power curves of $LG_{0,\pm m}$ mode laser under different m

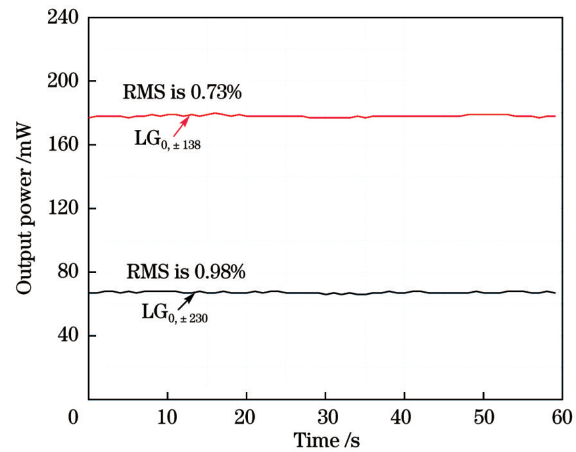

图7　$LG_{0,\pm 138}$ 和 $LG_{0,\pm 230}$ 模式激光的输出功率在60 s内的稳定性

Fig. 7　Stability of output power of $LG_{0,\pm 138}$ and $LG_{0,\pm 230}$ mode laser in 60 s

4　结　　论

基于腔内透镜球差的选模作用，得到了角向指数 m 可以便捷调控的超高阶 $LG_{0,\pm m}$ 模式涡旋激光。通过对高阶LG模式激光传输特性和光强分布的分析以及对透镜球差的计算，确定了表征激光输出镜位置和 $LG_{0,\pm m}$ 模式角向指数 m 关系的理论模型。实验中在2.06 W泵浦功率下获得了角向指数可大范围调谐且 m 最高可达280的超高阶 $LG_{0,\pm m}$ 模式涡旋光，激光输出具有良好的功率和模式稳定性。该方法所需的反射镜和球面透镜等器件均为通用的常规器件，易于获得、成本经济，适用于产生任意波长的LG模式激光。

参　考　文　献

[1] Willner A E, Huang H, Yan Y, et al. Optical communications using orbital angular momentum beams[J]. Advances in Optics and Photonics, 2015, 7(1): 66-106.

[2] Bradshaw D S, Andrews D L. Interactions between spherical nanoparticles optically trapped in Laguerre-Gaussian modes[J]. Optics Letters, 2005, 30(22): 3039-3041.

[3] Hnatovsky C, Shvedov V G, Krolikowski W, et al. Materials processing with a tightly focused femtosecond laser vortex pulse[J]. Optics Letters, 2010, 35(20): 3417-3419.

[4] 韦育, 于永河, 黑小兵, 等. 涡旋光束和光子计数在水下光通信中的应用[J]. 激光与光电子学进展, 2022, 59(13): 1301001.
Wei Y, Yu Y H, Hei X B, et al. Application of vortex beam and photon counting in underwater optical communication[J]. Laser & Optoelectronics Progress, 2022, 59(13): 1301001.

[5] Wang Z X, Zhang N, Yuan X C. High-volume optical vortex multiplexing and de-multiplexing for free-space optical communication[J]. Optics Express, 2011, 19(2): 482-492.

[6] 刘俊, 王健. 涡旋光激光器研究进展[J]. 中国激光, 2022, 49(12): 1201001.
Liu J, Wang J. Research progress of vortex laser[J]. Chinese Journal of Lasers, 2022, 49(12): 1201001.

[7] Fickler R, Lapkiewicz R, Plick W N, et al. Quantum entanglement of high angular momenta[J]. Science, 2012, 338(6107): 640-643.

[8] Emile O, Emile J. Naked eye picometer resolution in a Michelson interferometer using conjugated twisted beams[J]. Optics Letters, 2017, 42(2): 354-357.

[9] Beijersbergen M W, Coerwinkel R P C, Kristensen M, et al. Helical-wavefront laser beams produced with a spiral phaseplate[J]. Optics Communications, 1994, 112(5/6): 321-327.

[10] Beijersbergen M W, Allen L, van der Veen H E L O, et al. Astigmatic laser mode converters and transfer of orbital angular momentum[J]. Optics Communications, 1993, 96(1/2/3): 123-132.

[11] Courtial J, Padgett M J. Performance of a cylindrical lens mode converter for producing Laguerre-Gaussian laser modes[J]. Optics Communications, 1999, 159(1/2/3): 13-18.

[12] 柳强, 潘婧, 万震松, 等. 复杂涡旋结构光场的产生方法[J]. 中国激光, 2020, 47(5): 0500006.
Liu Q, Pan J, Wan Z S, et al. Generation methods for complex vortex structured light field[J]. Chinese Journal of Lasers, 2020, 47(5): 0500006.

[13] Omatsu T, Miyamoto K, Lee A. Wavelength-versatile optical vortex lasers[J]. Journal of Optics, 2017, 19(12): 123002.

[14] Chen Y F, Lan Y P, Wang S C. Generation of Laguerre-Gaussian modes in fiber-coupled laser diode end-pumped lasers[J]. Applied Physics B, 2001, 72(2): 167-170.

[15] 连天虹, 朱家华, 刘健宁, 等. 端面离焦泵浦薄片涡旋光激光器[J/OL]. 激光与光电子学进展: 1-11[2022-07-26]. https://kns.cnki.net/kcms/detail/31.1690.TN.20220724.1141.010.html.
LianT H, ZhuJ H, LiuJ N, et al. 端面离焦泵浦薄片涡旋光激光器[J/OL]. 激光与光电子学进展: 1-11[2022-07-26]. https://kns.cnki.net/kcms/detail/31.1690.TN.20220724.1141.010.html.

[16] Oron R, Danziger Y, Davidson N, et al. Laser mode discrimination with intra-cavity spiral phase elements[J]. Optics Communications, 1999, 169(1/2/3/4/5/6): 115-121.

[17] Ito A, Kozawa Y, Sato S. Generation of hollow scalar and vector beams using a spot-defect mirror[J]. Journal of the Optical Society of America. A, Optics, Image Science, and Vision, 2010, 27(9): 2072-2077.

[18] 李平, 张澍霖, 汪莎, 等. 通过优化损耗点镜产生高效率的涡旋光束[J]. 中国激光, 2020, 47(5): 0501005.
Li P, Zhang S L, Wang S, et al. High efficiency vortex beam generation by optimization of defect-spot mirror[J]. Chinese Journal of Lasers, 2020, 47(5): 0501005.

[19] Qiao Z, Xie G Q, Wu Y H, et al. Generating high-charge optical vortices directly from laser up to 288th order[J]. Laser & Photonics Reviews, 2018, 12(8): 1800019.

[20] Thirugnanasambandam M P, Senatsky Y, Ueda K. Generation of very-high order Laguerre-Gaussian modes in Yb:YAG ceramic laser[J]. Laser Physics Letters, 2010, 7(9): 637-643.

[21] Wang M, Ma Y Y, Sheng Q, et al. Laguerre-Gaussian beam generation via enhanced intracavity spherical aberration[J]. Optics Express, 2021, 29(17): 27783-27790.

[22] Sheng Q, Wang A H, Ma Y Y, et al. Intracavity spherical aberration for selective generation of single-transverse-mode Laguerre-Gaussian output with order up to 95[J]. PhotoniX, 2022, 3(1): 1-12.

[23] 王喜庆, 吕百达. 拉盖尔-高斯光束的聚焦特性[J]. 激光技术, 1996, 20(3): 185-190.
Wang X Q, Lü B D. Focusing properties of Laguerre-Gaussian beams[J]. Laser Technology, 1996, 20(3): 185-190.

[24] 盛泉, 耿婧旎, 王爱华, 等. 基于猫眼逆反射器的大范围免调试激光器[J]. 物理学报, 2023, 72(4): 044203.
Sheng Q, Geng J N, Wang A H, et al. Cat-eye retroreflectors based large-dynamic-range alignment-free laser[J]. Acta Physica Sinica, 2023, 72(4): 044203.

[25] Sheng Q, Wang A H, Qi Y, et al. Enhancing the field of view of cat-eye retroreflectors by simply matching the mirror radius of curvature and the lens focal length[J]. Results in Physics, 2022, 37: 105558.

[26] Siegman A E. Lasers[M]. Mill Valley: University Science Books, 1986, 16: 647.

[27] 刘俊杰, 盛泉, 王盟, 等. 基于腔内球差选模产生高阶拉盖尔-高斯模式激光[J]. 物理学报, 2022, 71(1): 014204.
Liu J J, Sheng Q, Wang M, et al. High-order Laguerre-Gaussian mode laser generated based on spherical aberration cavity[J]. Acta Physica Sinica, 2022, 71(1): 014204.

Ultra-High-Order Laguerre-Gaussian Vortex Laser via Mode-Selection Enabled by Intracavity Spherical Aberration

Wang Aihua[1,2], Li Jinhui[3], Sheng Quan[1,2*], Geng Jingni[1,2], Fu Shijie[1,2], Shi Wei[1,2**], Yao Jianquan[1,2]

[1]*School of Precision Instrument and Opto-Electronics Engineering, Tianjin University, Tianjin* 300072, *China*;
[2]*Key Laboratory of Opto-electronic Information Technology, Ministry of Education, Tianjin University, Tianjin* 300072, *China*;
[3]*Chengxian College, Southeast University, Nanjing* 210088, *Jiangsu, China*

Abstract

Objective Optical vortices in the Laguerre-Gaussian (LG) mode that have a unique hollow intensity profile and non-zero orbital angular momentum are highly significant for various applications. The LG mode laser can be generated using external-cavity devices, such as holograms or cylindrical lens pairs, to transform a Hermite-Gaussian beam into a LG beam, or using the intracavity, where the intracavity components are utilized to preferentially oscillate the certain high-order modes within a laser resonator. In comparison to the external-cavity approaches, intracavity approaches typically yield superior power handling, beam quality, and conversion efficiency. However, there are very few demonstrations regarding high-order LG mode laser oscillations with angular indices (m) beyond 30. The main challenge is that the beam patterns of the very-high-order mode lasers become highly complex, which makes it difficult to fabricate mode-selecting elements with a sufficient accuracy to precisely manage the loss and gain of a certain mode. In this study, we demonstrate the generation of an ultra-high-order LG mode output based on mode selection enabled by intracavity spherical aberration (SA). By calculating the focusing behavior of the high-order LG mode beam and the SA of the intracavity lens, the relationship between the angular indices m of the high-order $LG_{0,\pm m}$ vortex laser and the cavity parameters is determined. In the experiment, the ultra-high-order $LG_{0,\pm m}$ vortex lasers with tunable angular indices m of up to 280 are obtained with an end-pumped Nd: YVO_4 laser at a wavelength of 1064 nm, under an incident diode pump power of only 2.06 W.

Methods The experimental arrangement of the laser that generates the ultra-high-order LG mode output is depicted in Fig. 1. Two lenses, L1 and L2, with focal lengths of f_1=150 mm and f_2=51.8 mm, respectively, are inserted into the cavity of an end-pumped Nd: YVO_4 laser to collimate the beam and introduce SA for mode selection. The laser is pumped by a fiber-coupled diode laser at 878.6 nm, with a pump beam radius of approximately 120 μm at the input facet of the a-cut Nd : YVO_4 crystal and a Rayleigh length of approximately 0.9 mm. The crystal is located near the total reflector M1, while the distances between the crystal and lens L1 (d_1) and between lenses L1 and L2 (d_2) are 155 mm and 20 mm, respectively. The plano-concave input mirror M1 with a small radius of curvature of 50 mm generates a small beam waist near it, enabling the beam to expand significantly when it reached the lenses, thus enhancing the SA and resultant mode selection capability. The output coupler M2 is a flat mirror with a transmittance of 10% at 1064 nm. The beam waist position of the LG beam behind the focusing lens L2 can be obtained using Eq. (1). Considering that the beam arriving at lens L2 is well-collimated by lens L1, the relationship can be simplified as indicated in Eq. (3). Because the output coupler M2 is a flat mirror, the oscillating beam should have its waist exactly on the mirror surface. The defocused modes (with the beam waist deviated from M2) suffered a loss larger than that of the "on-focus" mode with the beam waist on M2. The spherical lens with SA is used as L2, and the focal length is not a constant but varies with the incident beam height. Therefore, mode selection can be achieved by adjusting the location of M2 within a small range to have different orders of modes focused on it. Moving the output coupler M2 toward lens L2 will result in modes with a larger m and vice versa.

Results and Discussions Figure 4 presents certain typical beam patterns recorded during the experiment. With an incident pump power of 2.06 W, the lowest order propagation-invariant single-mode $LG_{0,\pm m}$ mode laser is $LG_{0,\pm 38}$, which is obtained at distance between M2 and L2 of d_3=51.48 mm, and the highest order is $LG_{0,\pm 280}$, which is obtained at d_3=48.91 mm. The beams are petal-like because both the $+m$ and $-m$ components have a similar intensity, and the mode order can be determined by counting the surrounding dark bars. The high-order LG mode optical vortices demonstrate good mode purity and stability. Figure 5 presents the theoretical relationship of the mode order and the d_3 obtained using Eq. (3), as well as the experimental results, which sufficiently match the theoretical results. The slope efficiency of the laser decreases with the mode order owing to the increasing SA-induced cavity loss and decreasing mode matching.

Conclusions In summary, ultra-high-order LG mode vortex beams with selective angular indices are obtained by utilizing the SA of an off-the-shelf spherical lens in the laser cavity. By calculating the focusing behavior of the high-order LG mode beam and the SA of the intracavity lens, the relationship between the angular indices m of the high-order $LG_{0,\pm m}$ vortex laser and the cavity parameters is determined. In the experiment, an ultra-high-order $LG_{0,\pm m}$ vortex laser with tunable angular indices m of up to 280 is obtained with an end-pumped Nd : YVO_4 laser at a wavelength of 1064 nm, under an incident diode pump power of only 2.06 W. The ultra-high-order $LG_{0,\pm m}$ vortex laser exhibits good stability in terms of power and the transverse mode. The mode evolution in the experiment sufficiently matches with that in the theoretical model. This study provides theoretical and experimental references for the generation of ultra-high-order LG mode vortex lasers. By increasing the pump power or pump overlap to enhance the laser gain, arbitrary high-order modes can be expected using this method.

Key words laser optics; Laguerre-Gaussian mode; vortex laser; mode selection; high-order transverse mode; spherical aberration